PAPER

Check for updates

p-Phenyleneethynylene unit-conjugated dimeric zinc-phthalocyanines in bulk heterojunction solar cells: a comparative experimental and theoretical study†

Gülenay Tunç,[a] Gizem Gümüşgöz Çelik, [ID][a] Betül Canımkurbey, [ID][b]
Burcu Dedeoglu [ID][a] and Ayşe Gül Gürek [ID] *[a]

Nowadays, the photosensitivity of certain molecules, particularly phthalocyanines (Pcs), is well-studied. This field has made much progress, and several practical applications exist for these molecules. In this study, p-phenyleneethynylene-bridged two ZnPc dimers containing either bulky *tert*-butyl (**GT57**) or *tert*-butyl thiol (**GT60**) substituents at the peripheral position were synthesized as a novel donor component for bulk heterojunction (BHJ) solar cell applications. The molecular structure and photophysical properties of dimeric ZnPc derivatives were investigated by combined experimental and theoretical studies. The density functional theory (DFT) method was employed with B3LYP functional and the def2-SVP basis set to examine the designed complexes and calculate geometrical parameters and natural transition orbitals (NTOs). Additionally, the time-dependent density functional theory (TD-DFT) method was employed to investigate the optical properties through the analysis of UV-vis spectra. Dimeric ZnPc derivatives were blended as donor components alongside PCBM as the acceptor material in BHJ solar cells, achieving a maximum power conversion efficiency of 4.05%, for **GT60** and compared to **GT57**, cells based on **GT57** exhibited lower photovoltaic performance. These findings are encouraging and highlight the potential for further research on BHJ solar cells employing near-infrared-absorbing, non-aggregated dimeric ZnPc derivatives containing S heteroatoms.

Introduction

Phthalocyanines (Pcs) are commonly used as active components in organic photovoltaic (OPV) and hybrid dye-sensitized solar cells (DSSCs).[1–4] This is due to their unique electronic properties, distinctive chemical structure, and broad photo response range between 600 and 800 nm, which coincides with the region of maximum solar flux. As a result, only very thin films are required to absorb a significant portion of solar light. Pc-based OPVs can be fabricated either through vacuum evaporation or solution-processing techniques. However, unsubstituted Pcs are nearly insoluble in standard organic solvents because they tend to aggregate, making solution-based processing difficult. Despite this limitation, unsubstituted Pcs have been successfully used as active layers in vacuum-deposited small molecule solar cells.

On the other hand, chemically modified Pcs, which include substituents either at the peripheral or axial positions of the macrocycle, can be processed using solution-based techniques. These modifications not only adjust the electronic properties of the Pcs but also enhance their solubility in organic solvents.

In the case of solution-processed bulk heterojunction (BHJ) solar cells, only a limited number of examples involve soluble phthalocyanine (Pc) derivatives blended with soluble acceptor materials to form the BHJ active layer.[5–7] One such example, reported by Palomares *et al.*,[8] features a small molecule organic solar cell based on a soluble tetra-*tert*-butyl zinc phthalocyanine (ZnTBPc)/PCBM blend. This device achieved a short-circuit current density (J_{SC}) of approximately 3.57 mA cm^{-2}, an open-circuit voltage (V_{OC}) of about 0.53 V, and a power conversion efficiency (PCE) of roughly 0.77%. On the other hand, another group reported up to 1.6% efficiencies in solution-processed bulk heterojunction solar cells.[9] These cells utilized highly soluble ruthenium phthalocyanines (RuPcs) axially functionalized with pyridyl dendrons up to the third generation and blended with fullerene derivatives, such as PCBM or PC$_{71}$BM. The findings highlight that further advancements in the design of new Pc macrocycles are necessary to enhance their

[a] *Faculty of Science Department of Chemistry, Gebze Technical University, 41400 Gebze, Kocaeli, Turkey. E-mail: gurek@gtu.edu.tr*

[b] *Polatli Faculty of Arts and Sciences, Department of Physic, Ankara Hacı Bayram Veli University, 06900 Ankara, Turkey*

† Electronic supplementary information (ESI) available. See DOI: https://doi.org/10.1039/d5nj00636h

performance in BHJ solar cells. One key limitation contributing to the low efficiency of Pcs is their V_{OC}. Structural modifications to the Pc molecules, such as introducing different functional groups at specific positions, could help address this issue. These modifications aim to extend the absorption spectrum and fine-tune the electronic configuration of the excited states, offering promising strategies to improve the power conversion efficiency of solution-processed Pc-based BHJ solar cells.

A particularly promising approach that has gained traction in recent years is the synthesis of linker-bound dimeric phthalocyanine molecules. The incorporation of linkers, which are molecular bridges that connect phthalocyanine units, offers several advantages in optimizing the material properties for photovoltaic applications[10–12]

Linker groups significantly influence the intermolecular and intramolecular interactions of organic compounds in the solid state. As a result, they have garnered considerable attention in the synthesis of dimeric zinc(II) phthalocyanines. These groups play a crucial role in shaping the molecular and structural properties of the dimers, which, in turn, profoundly impact their functional and application-related characteristics.

Although the Pc system has garnered significant scientific and technological interest, the effort invested in developing multi-phthalocyanine arrays has been relatively limited[13–16] Nonconjugated Pc dyads have been documented as the two Pc cores being covalently connected via various types of bridges.[17] However, there are limited studies on Pc subunits connected through π-conjugated pathways.[18–23] Leznoff and colleagues synthesized the first Pc dimeric system featuring a butadiynyl bridge between the chromophores.[24] However, their method was limited to the preparating of homodimetallic bisphthalocyanines, resulting in low yield. Later, Torres et al. developed an efficient method for preparing homo- and heterodimetallic bisphthalocyanine complexes with ethynyl and butadiynyl bridges using metal-mediated coupling methodologies.[25] Göransson and colleagues then studied long-range electron transfer in zinc–phthalocyanine–oligo(phenylene-ethynylene)-based donor-bridge-acceptor dyads to understand the charge transfer mechanisms for solar energy conversion[26]

In recent years, zinc Pc dimers with various conjugated systems linking tri-tert-butyl phthalocyanine units have been synthesized as hole transport materials (HTMs) in organic–inorganic hybrid perovskite solar cells. These competitive HTMs linkers, to balance the trade of stability and performance[27] include 2,5-thienyl, 2,7-fluorenyl, 3,6-bisthienyl diketopyrrolopyrrole, and 1,4-phenyl.[10,28,29] Furthermore, Pc derivatives have also been utilized as a third component in polymer-fullerene-based BHJ solar cells to enhance the light-harvesting capacity of the photoactive layer.[30,31]

More recently, we have reported an oligo-(p-phenyleneethynylene) π-framework with proper functionalities and substituents could be an essential molecular family for high-efficiency solution-processed OLED devices.[32] Our previous study indicated that an oligo-(p-phenyleneethynylene)-framework is a promising linker group for photovoltaic applications, requiring a deeper analysis of the influence of the structure of used molecules on the final performance of OLED devices.

Building on these findings, the present paper focuses on synthesizing and characterizing of p-phenyleneethynylene-bridged two ZnPc dimers (**GT57** and **GT60**, Fig. 1) used in
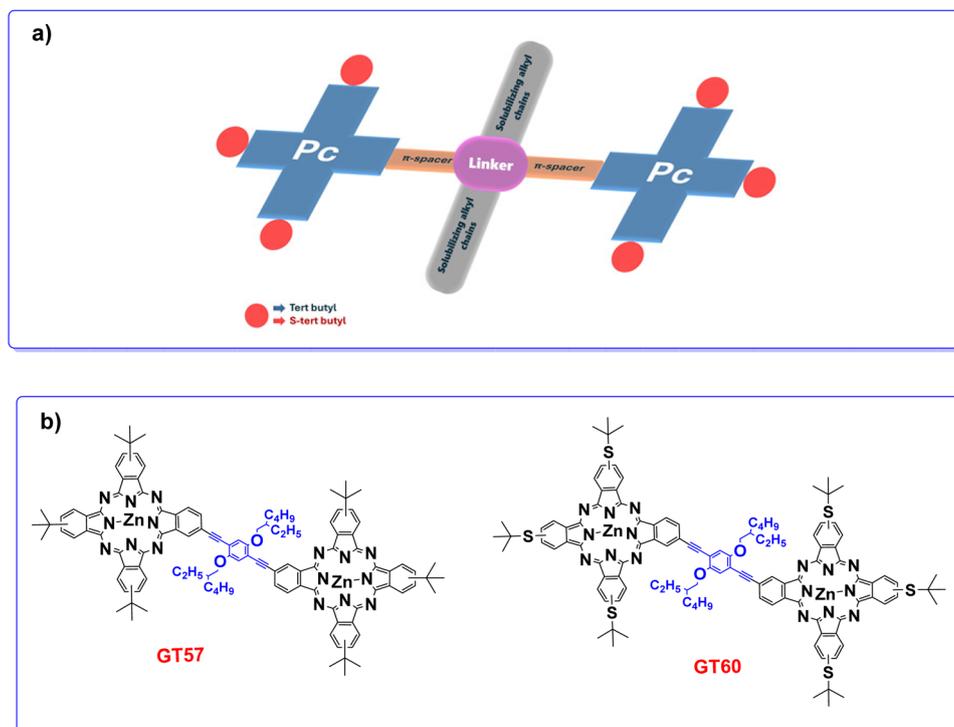

Fig. 1 (a) The molecular design of dimeric ZnPcs and (b) the corresponding chemical structures of **GT57** and **GT60**.

BHJ solar cells as new electron donor components. In this molecular structure, 2-ethylhexyloxy ($-OCH_2CH(C_2H_5)C_4H_9$) substituents on the bridged phenyl ring enhance solubility, enabling efficient synthesis, purification, and the fabrication of high-quality emissive films. The presence of swallow-tailed bulky substituents at the linker unit between two Pc molecules in a relatively small-sized molecular dimension is expected to impede undesired π–π interactions in the solid state that could otherwise yield excimer formation (redshift inemission) and induce nonradiative decay pathways (low quantum yield). Considering that the low photovoltaic performance of Pc-based BHJ solar cells may be linked to the inhomogeneous morphology of the active layer, characterized by the formation of large domains, the use of non-aggregated Pc can aid in achieving better control over the active layer morphology. Additionally, to gain deeper insight into the impact of sulfur atoms and six bulky *tert*-butyl substituents at the peripheral positions of dimeric Pcs on their photophysical and electrochemical properties, as well as their photovoltaic performance, theoretical calculations were performed.

1. Experimental

The 4-(*tert*-buthylthio)phthalonitrile (**PN3**)[33] and 1,4-bis(ethynyl)-2,5-bis(2-ethylhexyloxy)benzene (**L1**),[34] 2,9,16,23-tetra-*tert*-butyl-29*H*,31*H*-phthalocyanine (**TB4-ZnPc**)[35] and 2,9,16,23-tetra-*tert*-butyl-sulfanyl-29*H*,31*H*-phthalocyanine (**STB4-ZnPc**)[36] were synthesized

according to the literature. The equipment, materials, photophysical, electrochemical measurements, and spectra used for the characterization of the compounds are provided in the ESI.†

1.1. Synthesis

Synthetic pathways of **GT56**, **GT58**, **GT57**, **GT60** were given in Scheme 1.

1.1.1. Synthesis of GT56. This compound was synthesized following the procedure outlined in the literature.[25] 4-Iodophthalotrile (100 mg, 0.394 mmol), 4-(*tert*-butyl)phthalonitrile (507 mg, 2.34 mmol), and zinc acetate (183 mg, 1 mmol) were combined in 2 mL anhydrous dimethylaminoethanol (DMAE) in a reaction flask and were heated under reflux for 24 h. Subsequently, the solvent is removed from the reaction mixture under reduced pressure by evaporation. The resulting residue was washed several times with EtOH and water. The crude product was first purified by column chromatography by silica gel, followed by preparative thin-layer chromatography using an *n*-hexane:dioxane (4:1) mixture as eluent, yielding a blue solid designated as **GT56**. Yield: 82 mg (24%) ^{1}H NMR (500 MHz, d_6-DMSO) δ (ppm): 9.35–8.86 (m, 6H), 8.42–8.21 (m, 5H), 7.91–7.81 (m, 1H), 2.00–1.88 (m, 27H). ^{13}C NMR (125 MHz, d₆-DMSO) δ (ppm): 169.99, 158.44, 153.44, 153.14, 152.93, 152.57, 151.79, 150.22, 149.93, 149.28, 149.06, 138.86, 138.66, 138.14, 138.02, 137.02, 136.34, 136.12, 135.88, 133.36, 131.77, 130.59, 127.63, 127.48, 127.41, 127.36, 123.83, 123. 33, 122.66, 122.41, 121.86, 120.18, 119.12, 118.74, 118.40, 40.41
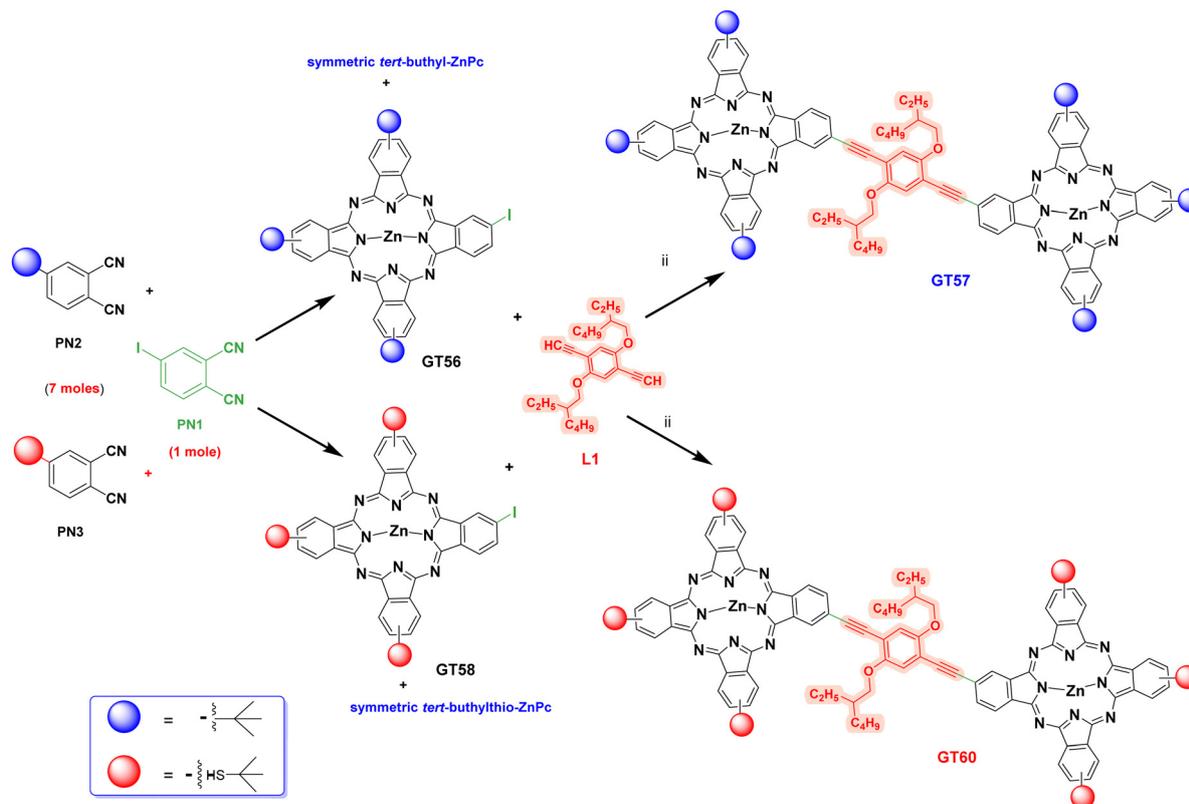
Scheme 1 Synthetic route of molecules (**GT56**, **GT57**, **GT58**, **GT60**). (i) DMAE$_{(dry)}$, Zn(OAc)$_2$, reflux, 24 h. (ii) Pd(PPh$_3$)$_2$Cl$_2$, CuI, THF, TEA.

(quaterner C), 36.21 (CH$_3$), 36.17 (CH$_3$), 36.15 (CH$_3$), 36.17 (CH$_3$), 36.12 (CH$_3$), 36.10 (CH$_3$), 36.00 (CH$_3$), 35.91 (CH$_3$). MALDI-TOF (m/z) calcd for C$_{44}$H$_{39}$IN$_8$Zn: 872.14; found: 871.735 [M]$^+$. Elemental analysis (%) calcd C, 60.60; H, 4.51; N, 12.85, found C 60.56; H, 4.60; N, 12.35.

1.1.2.   Synthesis of GT58. 4-Iodophthalonitrile (50.08 mg, 0.197 mmol), 4-(*tert*-butylthio)phthalonitrile (300 mg, 1.39 mmol), Zn(OAc)$_2$ (183 mg, 1 mmol) were dissolved in 2 mL anhydrous dimethylaminoethanol (DMAE). The reaction mixture was heated to reflux and stirred for 24 hours. The solvent is removed from the reaction mixture under reduced pressure by evaporation. The resulting residue was washed several times with EtOH and water. The resulting solid product was first purified by column chromatography on silica gel, followed by preparative thin-layer chromatography using *n*-hexane:dioxane (3:1) mixture as the mobile phase, yielding **GT58** as a blue color solid. Yield: 60 mg (31%). ^{1}H NMR (500 MHz, d_6-DMSO) δ (ppm): 9.31–8.72 (m, 6H), 8.59–8.14 (m, 6H), 1.82–1.61 (m, 27H). ^{13}C NMR (125 MHz, d_6-DMSO) δ (ppm): 171.94, 171.10, 154.53, 153.98, 145.99, 140.78, 140.47, 140.09, 137.45, 136.37, 134.49, 133.72, 133.33, 128.03, 127.70, 126.06, 125.18, 124.88, 110.97, 105.14, 99.06, 49.93 (quaterner C), 34.33 (CH$_3$). MALDI-TOF (m/z) calcd for C$_{44}$H$_{39}$I$_3$N$_8$S$_3$Zn: 966.08; found: 968.320 [M + 2H]$^+$. Elemental analysis (%) calcd C, 54.58; H, 4.06; N, 11.57, found C, 54.36; H, 4.58; N, 11.34.

1.1.3.   Synthesis of GT57. GT56 (20 mg, 0.023 mmol), 1,4-bis(ethynyl)-2,5-bis(2-ethylhexyloxy)benzene (**L1**) (2.87 mg, 0.0075 mmol), CuI (2.4 mg, 0.0012 mmol) and Pd(PPh$_3$)$_2$Cl$_2$ (9.6 mg, 0.0013 mmol) were dissolved in a mixture of 3 mL anhydrous tetrahydrofuran (THF) and 3 mL triethylamine (TEA) under argon atmosphere. The reaction mixture was stirred at 60 °C for 48 h. After that, the reaction mixture is extracted with dichloromethane and water. The organic phase was separated, dried over Na$_2$SO$_4$, and filtered. The solvent was removed by evaporation, and the resulting solid product was purified by preparative thin-layer chromatography using hexane:dioxane (4:1) mixture as the mobile phase, yielding **GT57** as a green solid (12 mg 85%). FT-IR (ATR) ν_{max}/cm^{-1} 3054 (ArC-H), 2958–2860 (aliphatic CH), 2106.5 (C≡C), 1653.2, 1611.7, 1485.8, 1460.2, 1436.7, 1389.6, 1328.4, 1257.3, 1148.3, 1044.8, 1024.4, 919.8, 827.2, 799.9, 747.4, 720.2, 691.3, 674.1. ^{1}H NMR (500 MHz, d_8-THF) δ (ppm): 9.50–9.18 (m, 16H, ArH), 8.34–8.21 (m, 8H, ArH), 7.50 (brs, 2H ArH), 4.38, 4.34 (s, 4H, OCH$_2$) 2.01–1.86 (m, 56H, CH$_3$), 1.45 (m, 8H), 1.32 (m, 8H), 1.06–0.97 (m 12H, CH$_3$). ^{13}C NMR (125 MHz, d_8-THF) δ (ppm): 154.47, 152.76, 151.35, 145.92, 145.25, 138.99, 138.33, 136.68, 131.35, 125.50, 124.15, 122.37, 119.03, 116.56, 114.48, 112.70, 96.25, 93.26, 72.91, 71.96, 53.13, 40.29, 35.65, 31.67, 31.02, 29.67, 24.83, 23.37, 13.74, 11.38. MALDI-TOF (m/z) calcd for C$_{114}$H$_{114}$N$_{16}$O$_2$Zn$_2$: 1873.04; found: 1871.015 [M-2H]$^+$. Elemental analysis (%) calcd C, 73.18; H, 6.14; N, 11.98, found C, 73.01; H, 6.44; N, 11.55.

1.1.4.   Synthesis of GT60. GT58 (18 mg, 0.0185 mmol), 1,4-bis(ethynyl)-2,5-bis(2-ethylhexyloxy)benzene (**L1**) (2.37 mg, 0.0061 mmol), CuI (2.4 mg, 0.0012 mmol) and Pd(PPh$_3$)$_2$Cl$_2$ (9.6 mg) (0.0013 mmol) were dissolved in a mixture of 3 mL anhydrous tetrahydrofuran (THF) and 3 mL triethylamine (TEA)

under argon atmosphere. The reaction mixture was stirred at 50 °C for 48 h. After that, the reaction mixture was extracted with dichloromethane and water. The organic phase was separated, dried over Na$_2$SO$_4$, and filtered. The solvent was removed by evaporation, and the resulting solid product was purified by preparative thin-layer chromatography using hexane:ethanol (10:1) mixture as the mobile phase, yielding **GT60** as a green solid (11 mg, 86%). FT-IR (ATR) ν_{max}/cm^{-1} 3000 (ArC–H), 2925–2862 (aliphatic CH), 2105.4 (C≡C), 1605.0, 1485.8, 1388.9, 1363.1, 1334.3, 1256.8, 1138.8, 1041.4, 908.4, 832.1, 745.1, 685.2. ^{1}H NMR (500 MHz, d_8-THF-) δ (ppm): 9.16–9.10 (m, 6H, ArH), 8.37–832 (m, 4H, ArH), 7.47–7.42 (m, 16H, ArH), 4.76 (brs, 4H, OCH$_2$), 2.06 (s, 54H, CH$_3$), 1.64–1.62 (m, 10H, CH$_2$ + CH), 1.29 (m 8H, CH$_2$), 0.91–0.88(m, 12H, –CH$_3$) ^{13}C NMR (125 MHz, d_8-THF) δ (ppm): 164.92, 153.09, 138.68, 137.97, 135.14, 134.60, 133.59, 131.32, 129.23, 128.01, 127.94, 122.22, 97.20, 89.94, 56.96, 53.74, 46.23, 39.11, 31.90, 30.85, 29.67, 29.39, 28.97, 23.99, 22.59, 22.29, 13.46, 10.44. MALDI-TOF (m/z) calcd for C$_{114}$H$_{114}$N$_{16}$O$_2$S$_6$Zn$_2$: 2063.401; found: 2063.493 [M]$^+$. Elemental analysis (%) calcd C, 66.36; H, 5.57; N, 10.86, found C, 66.14; H, 5.61; N, 10.46.

2. Results and discussion

2.1.   Synthesis and structural characterization

The key to the synthesis of ethynyl-bridged dimeric phthalocyaninate complexes *via* metal-mediated coupling is the availability of an asymmetric iodo phthalocyanine and a linker with appropriately functionalized ethynyl groups such as **L1** (Fig. 1). This study reports the synthesizing of dimeric zinc phthalocyanines (**GT57, GT60**) using 1,4-bis(ethynyl)-2,5-bis(2-ethylhexyloxy)-benzene as a linker between two Pc units (Fig. 1). The synthesis of dimeric phthalocyanines **GT57** and **GT60** was carried out in two steps following the routes depicted in Scheme 1. Firstly, the asymmetric iodo-*tert*-buthyl or iodo-*tert*-butylthio phthalocyanine derivatives (**GT56, GT58**) were obtained utilizing by the cyclotetramerization reaction of iodophthalonitrile (**PN-1**) with other phthalonitriles (**PN-2** and **PN-3**) in a molar ratio of 1:7, respectively. The phthalonitrile derivatives were used in a 1:7 molar ratio, resulting in the formation of only two products: the desired mono-iodinated asymmetric phthalocyanine derivatives (**GT56** or **GT58**) and symmetric phthalocyanine derivatives containing *tert*-butyl groups, as outlined in Scheme 1. In the final, Sonogashira cross-coupling step, the dimeric phthalocyanine derivatives (**GT57, GT60**) were subjected to reactions with mono-iodophthalocyanines **GT56** or **GT58** and 1,4-bis(ethynyl)-2,5-bis(2-ethylhexyloxy)-benzene (**L1**) as linker group in the presence of a Pd(PPh$_3$)$_2$Cl$_2$ catalyst and a CuI/Et$_3$N co-catalyst/base system in THF, resulting in the formation of the desired products with a yield of 85% and 86% (**GT57, GT60**) respectively. Highly selective Sonogashira cross-coupling at the iodo-functionalized reaction site was utilized in this process. The selectivity undoubtedly arises from the better reactivity of iodine atoms as compared to others. This facilitates the rate-determining oxidative addition step in the catalytic cycle.

Despite its large molecular weight, Pc derivatives were found to be soluble in common organic solvents such as chloroform and THF, as well as printing-friendly solvents such as toluene. Pcs were purified by thin layer chromatography on silica gel using dioxane : n-hexane (1 : 3, v/v) solvent mixture. All new compounds were fully characterized using ^{1}H–^{13}C-NMR, MALDI TOF-MS, and FTIR, and optically evaluated by UV/vis and steady-state fluorescence emission spectroscopies Fig. S1–S25 (ESI†).

^{1}H NMR spectra recorded in [d$_8$]THF are very well resolved and all the different protons could be assigned (see the ESI†). However, although the system in which two units of ZnPc are bonded to the L1 moiety, GT57 and GT60, are quite soluble in THF, broad signals were obtained in the ^{1}H NMR spectra even when using a coordinating solvent such as [d$_8$]THF due to the high degree of π–π-stacking and also to the presence of too many regioisomers (see the Fig. S12, S13, S17 and S18, ESI†). Phthalocyanines tend to form aggregates in solutions. Aggregation causes molecules to move closer together, changing the chemical environment of the protons. This can result in broad, indeterminate, and unresolved peaks in the spectrum. However, the integrated signal intensities reflect the number of hydrogen atoms in the compounds.

MALDI-TOF MS spectra are important for verifying the structure of phthalocyanines. The MALDI-TOF MS spectra of the purified monofunctional Pcs were detected molecular ion peaks at m/z 871.735 [M]$^+$, 968.320 [M]$^+$, for GT56, GT58, and 1871.015 [M]$^+$ and 2063.493 [M]$^+$ for GT57 and GT60, respectively (Fig. S2, S6, S11 and S16, ESI†). The absence of signals corresponding to other substituted derivatives in the mass spectra provides significant support for the structural purity of the compounds. Each spectrum offers compelling evidence that reinforces the validity of their proposed structures.

2.2. Photochemical and photophysical measurements

The photophysical and photochemical properties of the prepared dimeric ZnPcs were extensively evaluated using UV-vis absorption, steady-state fluorescence, and time-resolved fluorescence spectroscopies. The UV-vis absorption and fluorescence spectra of the GT57 and GT60 were investigated in the 300–800 nm range using different solvents such as toluene, THF, dioxane, DMSO, and DMF to evaluate their aggregation properties and their

photophysical and photochemical characteristics. THF was chosen for the photophysical and photochemical measurements among these solvents due to its superior solubility and the absence of significant changes with solvent variation. All spectral data, including UV-vis spectra obtained at different concentrations in THF, are provided in the ESI† (Fig. S19 and S20).

Fig. 2 shows the absorption spectra of the dimers and monomeric ZnPcs (TB4-ZnPc and S-TB4-ZnPc) dissolved in THF. As can be seen, the Soret bands of both dimeric ZnPc derivatives are observed between 300 and 400 nm, while the Q bands of GT57 and GT60 exhibit a bathochromic shift and increased bandwidth compared to their monomeric counterparts, TB4-ZnPc (672 nm)[29] and S-TB4-ZnPc (678 nm),[36] respectively, due to the more extended conjugation of these systems. In addition, the Q-band maxima of dimer GT57 is split in two peaks in THF solution (Fig. 2a). This is likely caused by the presence of regioisomers and their non-symmetric nature[29,37,38] Typically, enhanced molecular stacking results in broader absorption signals and a reduced molar extinction coefficient (ε) due to decreased absorption intensity. However, this trend does not hold for dimer GT60, as the presence of the tert-butyl thio moieties consisting bulky tert-butyl and S heteroatoms on two Pc macrocycles reduces molecular aggregation, resulting in a strong single Q-band at 679 nm.

The various solvents were employed to examine the fluorescence emission properties of dimeric ZnPcs (Fig. S21–S25, ESI†). While no significant changes were observed in the fluorescence of the GT60 compound in different solvents, the GT57 compound exhibited strong fluorescence in low-polarity solvents such as THF, dioxane, and toluene. However, a significant decrease in fluorescence intensity was observed in high-polarity solvents like DMF and DMSO. This behavior is attributed to the tendency of high-polarity solvents to promote molecular aggregation or facilitate intermolecular energy transfer, leading to fluorescence quenching. Emission maximums of GT57 and GT60 are observed at 702 nm and 687 nm, in THF respectively.

The fluorescence quantum yield (Φ_F) is a key parameter that reflects the efficiency of the fluorescence process and is essential for photophysical applications.[39] To calculate the fluorescence quantum yields in THF, the fluorescence area integration
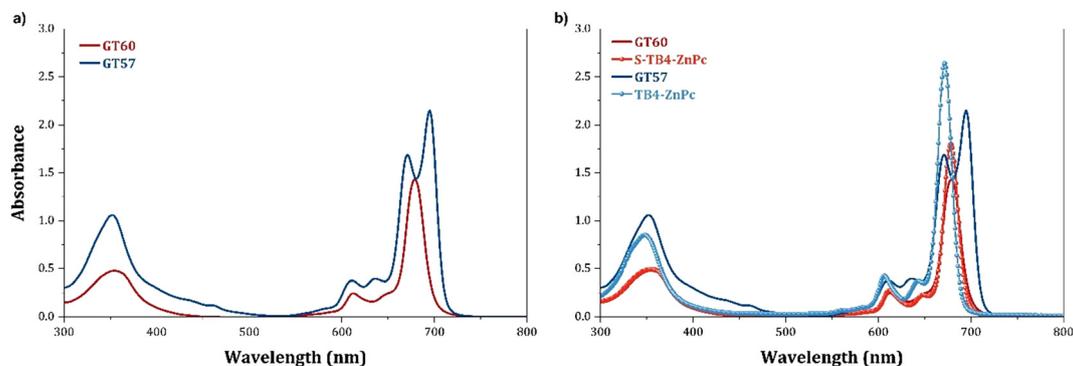

Fig. 2 (a) UV-vis absorption spectra of dimeric ZnPc derivatives (GT60 and GT57) (b) TB4-ZnPc, S-TB4-ZnPc, GT60, GT57 in THF.
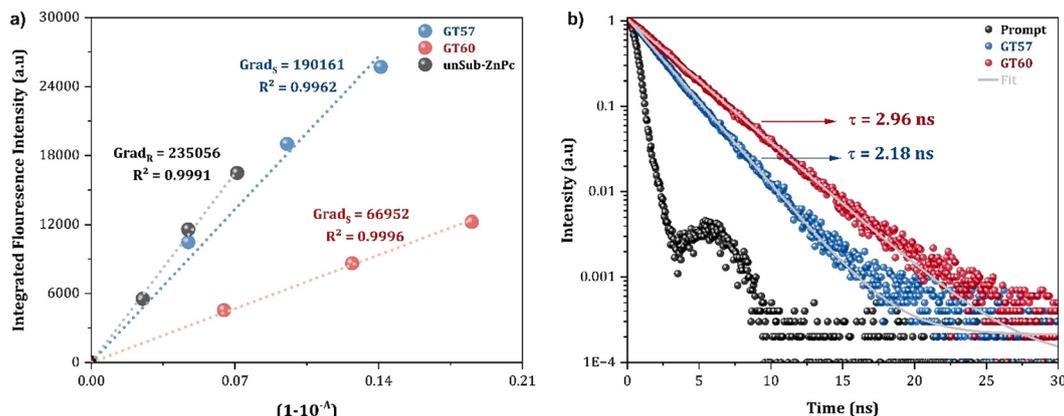
Fig. 3 (a) Fluorescence area integrates *vs.* absorbance of **GT57**, **GT60** and **Unsub-ZnPc** (b) fluorescence decay curves of **GT57** and **GT60** in THF (NanoLed λ_{ex}: 674 nm).

of the dimeric ZnPc derivatives (**GT60** and **GT57**) and the reference **Unsub-ZnPc** ZnPc *vs.* absorbance were plotted (Fig. 3a). Table 1 shows the obtained fluorescence quantum yields. Φ_F values of dimeric ZnPcs **GT57** and **GT60** were determined to be 0.20 and 0.08 which were lower than that of **Unsub-ZnPc**. respectively, by the absolute method using an integrating sphere.

Time-resolved fluorescence measurements quantify fluorescence lifetime (τ_F). The fluorescence lifetimes of **GT57** and **GT60** were measured in ambient conditions using the time-correlated single photon counting (TCSPC) technique in THF. Both molecules showed single exponential decay, obtaining the values of $\tau_F = 2.18$ ns for **GT57** and $\tau_F = 2.96$ ns for **GT60** (Fig. 3b). These values indicate that there is no significant difference between the fluorescence lifetimes of dimeric phthalocyanine derivatives (**GT57** and **GT60**) and the standard **Unsub-ZnPc**.

The singlet oxygen generation quantum yield (Φ_Δ) represents the number of singlet oxygen molecules produced per photon the photosensitizer absorbs. Optical determination of singlet oxygen was carried out using a direct measurement technique. The direct method involves detecting the intrinsic phosphorescence of singlet oxygen using a near-IR sensitive detector. After excitation with a xenon-arc source at the respective absorption maxima, the phosphorescence spectra of singlet oxygen were recorded for four phthalocyanines in THF at equal absorbance (0.23) to determine Φ_Δ directly (Fig. S26, ESI†). The **Unsub-ZnPc** was used as the reference (Table 1). The highest Φ_Δ value, observed for the dimer **GT60** complex (0.74), indicates efficient energy transfer to molecular oxygen, which may be linked to its UV behavior. In contrast, **GT57** demonstrates

singlet oxygen generation comparable to **Unsubs-ZnPc**, confirming their potential for triplet photosensitized applications.

2.3. Electrochemical measurements

The electrochemical behavior of MPcs was investigated using cyclic voltammetry (CV) to determine the HOMO (highest occupied molecular orbital)–LUMO (lowest unoccupied molecular orbital) energy level. The measurements were performed using a three-electrode system, consisting of a glassy carbon electrode (GCE) as the working electrode, a platinum wire as the counter electrode, and an Ag/AgCl aqueous electrode as the reference electrode. MPcs were prepared at a concentration of 5×10^{-4} M, and all experiments were conducted in THF at 25 °C, with 0.1 M NBu_4PF_6 (tetrabutylammonium hexafluorophosphate) used as the supporting electrolyte. Before measurements, the solution was purged with $N_{2(g)}$ for 5 minutes. The ferrocene/ferrocenium (Fc/Fc^+) redox couple was employed as an internal standard. CVs were recorded at a 100 mV s^{-1} scan rate and used to calculate the HOMO–LUMO energy level. The voltammograms were referenced against the Fc/Fc^+ redox couple and calculated with 4.8 eV below the vacuum level set as the reference level, as shown in Fig. 4.

Zn(II) phthalocyanines essentially showed ligand-centered redox reactions instead of metal-centered ones. Oxidation and reduction processes include electron transfer inside the π-conjugated system. In this case, the initial redox couple identified in the negative scan correlates to the LUMO level, whereas the first redox couple detected in the positive scan corresponds to the HOMO level. The HOMO energy levels of the dimeric phthalocyanine compounds were determined as

Table 1 Photophysical and photochemical parameters in THF

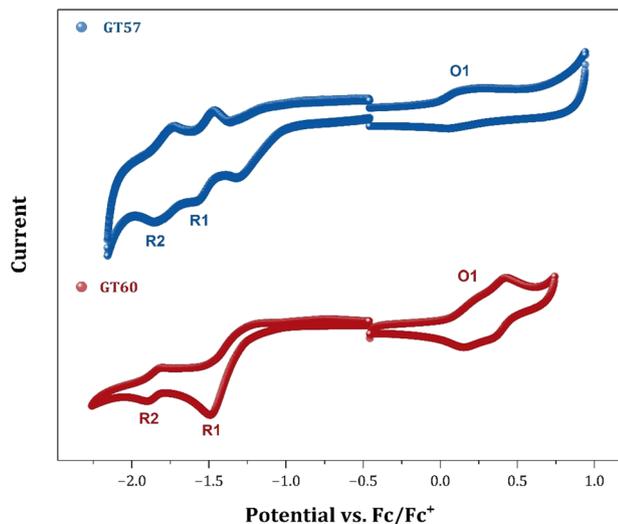| Compound	λ_{max}^{abs} (nm)	Log ε	λ_{max}^{em} (nm)	λ_{ex} (nm)	Φ_F	Φ_Δ^{direct}	τ_F (ns)
GT57	695	5.33	702	650	0.20	0.50	2.18
	671	5.22					
GT60	679	5.15	687	645	0.08	0.74	2.96
Unsub-ZnPc	666[40]	5.19[40]	673[40]	635[40]	0.25[40]	0.53[41]	2.72[40]

Fig. 4 CVs of **GT57** and **GT60** at 100 mV scan rate on GCE in THF$_{(dry)}$/0.1 M TBAP at 25 °C.

-4.98 and -5.10 eV while their LUMO levels were found to be -3.28 eV and -3.45 eV for **GT57** and **GT60**, respectively. According to Molina *et al.*, the energy levels of the monomeric ZnPc derivative (**TB4-ZnPc**) were determined to be -5.05 eV and -3.26 eV.[29] No significant change was observed in the energy levels between the dimeric **GT57** and the monomeric **TB4-ZnPc** phthalocyanine derivatives.

2.4. Theoretical calculations

2.4.1. Computational details. All calculations were performed with the Gaussian 16 program package.[42] Geometry optimizations were carried out using the density functional B3LYP,[43–45] known for its accuracy in reproducing geometries, along with the long-range corrected functionals CAM-B3LYP[46,47] and wB97XD,[48] employing the def2-SVP basis set. The optimized structures are shown in Fig. S27 (ESI†). The geometries optimized with B3LYP and CAM-B3LYP exhibit structurally similar elongated forms. However, the wB97XD functional overestimated weak interactions, leading to a sandwich-like structure due to CH/π hydrogen bond interactions.

The HOMO–LUMO band gap was calculated for these optimized structures and compared with experimental values (Table S1, ESI†). While CAM-B3LYP and wB97XD overestimated the band gap, B3LYP provided results closest to the experimental data. Additionally, the performance of this methodology in previous studies on macrocyclic systems showed good agreement between theoretical and experimental results.[36] Based on both the current benchmark study and our prior experience, B3LYP with the def2-SVP basis set was selected for geometry optimizations in this study. All stationary points have been characterized by a frequency analysis at the same theory level as the geometry optimizations.

The UV-vis electronic absorption spectra in the solution phase were computed using the time-dependent DFT (TD-DFT) method.[49] Two different functionals were employed: CAM-

B3LYP/def2-SVP, based on ground-state geometries optimized at the same level, and TPSSh/def2-SVP, based on geometries optimized at the B3LYP/def2-SVP level (Table S2, ESI†). The CAM-B3LYP method was chosen due to its established accuracy in excited-state predictions in solar cell applications.[47,50,51] However, the results obtained from both functionals were comparable. Since TPSSh had previously been used in similar zinc phthalocyanine systems, we selected this functional to maintain consistency with our earlier study.[52] The solvent was modeled using the integral equation formalism model (IEFPCM)[53–56] and tetrahydrofuran (THF) was used, as it was as the solvent employed in the experimental part of this study.

In TD-DFT, excited states are depicted as a linear combination of excitations from occupied to virtual Kohn–Sham orbitals. This expression in terms of molecular orbitals can be complicated, as numerous occupied and virtual orbital pairs may contribute to the expansion with comparable significance. An enhancement for gaining a more profound comprehension of the physical characteristics of electronic transitions relies on depicting an excited state through natural transition orbitals (NTOs).[57] Thus, NTOs have been computed as implemented in Gaussian.

2.4.2. Molecular structure. Dimeric zinc phthalocyanine with 1,4-bis((2-ethylhexyloxy)-2,5-diethylbenzene) (**GT57**, **GT60**) can exist in several isomeric configurations due to the numerous possible positions of the substituted groups. We select one isomer as a model based on steric requirements to represent all and evaluate the molecular and electronic structures of these isomers for the system examined in this study. The geometries of both molecules are optimized to precisely anticipate their properties and behavior. The optimized structures are depicted in Fig. 5. Both structures present a planar macrocycle with slight differences in angles of the substituents (*tert*-butyl and *tert*-butylthio).

The frontier molecular orbitals (HOMO and LUMO) offer essential insights into the chemical behavior, of the systems under investigation. For **GT57**, both the HOMO and LUMO are delocalized across the dimer, including the bridge, and exhibit a π–π* character (Fig. S28, ESI†). A similar delocalization and electronic nature are also observed for **GT60**. The calculated HOMO energy values are slightly underestimated, while the LUMO energies are slightly overestimated (Table 3). Although the calculated bandgap values are similar, the bandgap of **GT57** is slightly lower than that of **GT60**, which is consistent with the experimental values (Table 2).
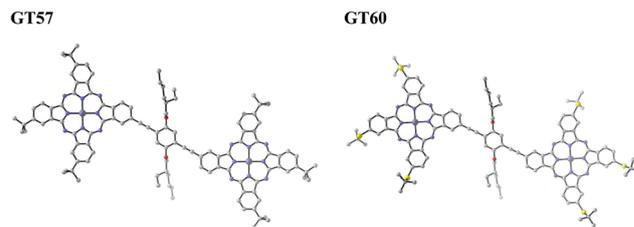

Fig. 5 Optimized molecular structures of **GT57** and **GT60** calculated at the B3LYP/def2-SVP level of theory in the gas phase. Hydrogen atoms are omitted for clarity.

Table 2 HOMO and LUMO energy level values were determined from experimental cyclic voltammetry (CV), and band gap energy values were found from UV-vis measurement

Compounds	R1[a]	O1[a]	$\Delta E_{1/2}$[b] (V)	HOMO[c] (eV)	LUMO[d] (eV)	E_{opt} (V)
GT57	−1.52	0.18	1.70	−4.98	−3.28	1.75
GT60	−1.35	0.30	1.65	−5.10	−3.45	1.77

[a] $E_{1/2} = (E_{pa} + E_{pc})/2$ at 0.100 V s^{-1}. [b] $\Delta E_{1/2} = E_{1/2}$ (first oxidation) $- E_{1/2}$ (first reduction) = HOMO–LUMO gap. [c] $E_{HOMO} = -[(E_{ox} - E_{1/2(ferrocene)}) + 4.8]$. [d] $E_{LUMO} = -[(E_{red} - E_{1/2(ferrocene)}) + 4.8]$.[58]

Table 3 Theoretical HOMO, LUMO and band gap energies of **GT57** and **GT60**

Compounds	E_{HOMO} (eV)	E_{LUMO} (eV)	ΔE (eV)
GT57	−5.02	−2.98	2.05
GT60	−5.29	−3.23	2.07

We also analyzed the molecular electrostatic potential (MEP) of the molecules, which provides insights into their electron-rich and electron-poor regions. Fig. 6 displays the electrostatic potential maps for **GT57** and **GT60**. An electrophilic region (shown in blue) on the zinc denotes an electron-poor site on the metal atom, which is as expected. In **GT60**, the zinc atom is more electrophilic due to the presence of *tert*-butylthio substituents. The NPA charges of the metal atoms in **GT57** and **GT60** are 1.261 and 1.263, respectively. In contrast, the linker exhibits a strong nucleophilic character, indicated in red.

2.4.3. Optoelectronic properties. The computed absorption spectra **GT57** and **GT60** convoluted using Gaussian functions are reported in Fig. 7. In **GT57** and **GT60**, there is a strong absorption at around 650 nm, which corresponds to the Q bands. There is also a weaker peak near 400 nm that is related to the B band. Aside from the small red and blue shifts for the B and Q bands observed in the theoretical absorption spectrum, these results align with the experimental findings shown in Fig. 6.

The nature of the different excited states can be easily determined by analyzing the corresponding Natural Transition Orbitals (NTOs) (Fig. S29, ESI†). The occupied and virtual NTOs for the transitions in the Q band indicate that these transitions are primarily attributed to a π–π* localization within the phthalocyanine rings, with noticeable delocalization present in both the occupied and virtual NTOs involving the substituents. For the transition responsible for the 400 nm absorption, the occupied and virtual NTOs of **GT57** are mainly delocalized
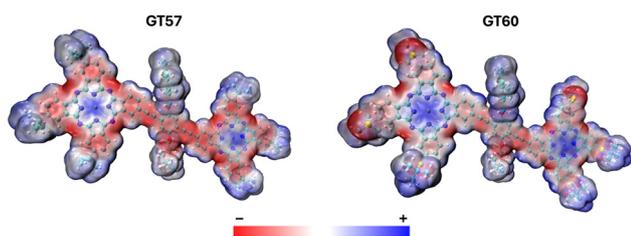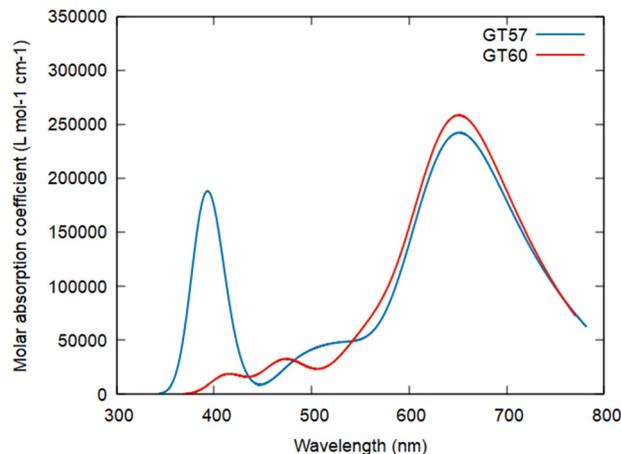

Fig. 7 TD-DFT (TPSSh/def2-SVP) predicted absorption spectra for **GT57** and **GT60** in THF.

over the linker and the benzene substituent connected to the linker of the phthalocyanine. For **GT60**, we observe two less intense peaks around 415 and 473 nm. For 415 nm transitions, occupied NTOs are delocalized over the linker involving the benzene substituents whereas the virtual NTOs are localized over the phthalocyanine ring. The parameters obtained from TD-DFT calculations are summarized in Table 4.

2.5. Solar cell device performance

Organic solar cells (OSCs) have garnered significant interest as a cost-effective solution for photovoltaic energy generation. The introduction of the bulk-heterojunction (BHJ) concept has notably improved OSC performance by effectively blending electron donor and acceptor materials into a solution, which is subsequently deposited as a thin film between two electrodes. Over the last decade, substantial advancements have been achieved in enhancing the power conversion efficiency (PCE) of organic BHJ solar cells.

In this study, OSCs with the structure ITO-ZnO/P3HT:**GT57**-**GT60**:PCBM/MoO$_3$/Al were fabricated, as illustrated in Fig. 8a. Fig. 8 provides an overview of the device architecture, energy band diagram, and the relationship between current density and applied voltage. Current density–voltage (J–V) measurements were conducted using a Keithley 4200 semiconductor characterization system, with a 100 mW cm^{-2} solar simulator (Thermo Oriel, AM 1.5G) serving as the light source. The photovoltaic parameters of the devices, derived from three distinct

Fig. 6 Electrostatic potential maps of **GT57** and **GT60**.

Table 4 Calculated parameters of the electronic absorption spectra in the solution phase (THF): dipole moment, wavelength, energy and oscillator strength

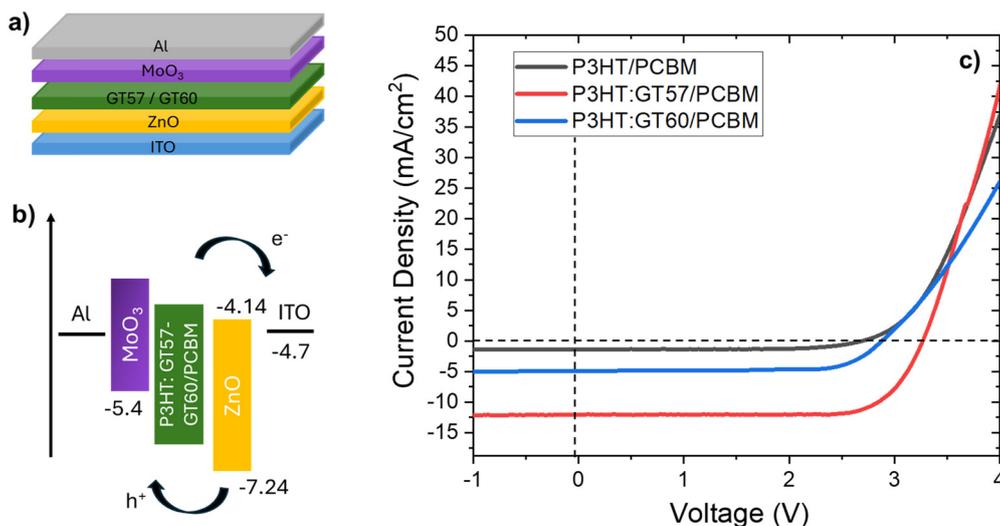| Compounds	μ (D)	λ (nm)	E (eV)	f
GT57	0.48	660	1.88	1.699
		391	3.17	1.115
GT60	0.31	654	1.90	1.600
		473	2.62	0.3514
		415	2.99	0.1515

Fig. 8 (a) Device structure (b) energy level of materials (c) typical J–V curves of P3HT/PCBM, P3HT:**GT57**/PCBM, P3HT:**GT60**/PCBM solar cell devices.

blend compositions, are summarized in Table 5, where each parameter represents the average of 24 devices. Representative J–V curves for the fabricated devices are also compared in Fig. 8.

The reference P3HT:PCBM device exhibited a V_{OC} of 2.67 V, a J_{SC} of 1.43 mA cm^{-2}, and a fill factor (FF) of 0.56, consistent with reported literature values[59,60] Incorporating **GT57** and **GT60** into the P3HT blend resulted in a significant enhancement in J_{SC}, with only a minor change in FF, leading to PCEs of 3.87% and 4.05% for the P3HT:**GT57**/PCBM and P3HT:**GT60**/PCBM devices, respectively (Table 5). Notably, the P3HT:**GT60**/PCBM device demonstrated an approximately 25% increase in J_{SC} compared to the reference P3HT:PCBM device, underscoring the effectiveness of the material modifications.

The primary performance parameters of organic solar cells include short-circuit current density (J_{SC}), open-circuit voltage (V_{OC}), fill factor (FF), and efficiency (η). The J_{SC} and V_{OC} values are derived from the intersections of the current density–voltage (J–V) curve with the respective axes. The maximum power point (MPP) is identified from the power–voltage (P–V) curve, allowing for the calculation of I_{MP} and V_{MP}. The fill factor and efficiency are computed using the following equations.[59]

$$\mathrm{FF} = \frac{J_{\mathrm{mpp}} V_{\mathrm{mpp}}}{J_{\mathrm{SC}} V_{\mathrm{OC}}},$$

$$\eta = \% \frac{J_{\mathrm{SC}} V_{\mathrm{OC}} \mathrm{FF}}{P_{\mathrm{S}}}.$$

where P_{S} is the power of incident light.

Table 5 Performance parameters of P3HT/PCBM, P3HT:**GT57**/PCBM, P3HT:**GT60**/PCBM solar cell devices

Vices	FF (%)	V_{OC} (V)	J_{SC} (mA cm^{-2})	η (%)
P3HT/PCBM	0.56	2.67	1.43	3.68
P3HT:**GT57**/PCBM	0.58	2.88	4.91	3.87
P3HT:**GT60**/PCBM	0.63	3.26	12.09	4.05

The surface morphology of the active layers was investigated using scanning electron microscopy (SEM) (Fig. 9a and b) and atomic force microscopy (AFM). Fig. 9c and d show the root-mean-square (RMS) roughness values of 1.92 nm for the P3HT:**GT57**/PCBM blend film and 1.35 nm for the P3HT:**GT60**/PCBM blend film, respectively. These results indicate a high level of miscibility between the donor materials and the PCBM acceptor. Notably, the P3HT:**GT60**/PCBM blend film exhibits reduced surface roughness and more pronounced bicontinuous phase separation. This well-defined morphology enhances the interfacial area between the donor and acceptor materials, improving exciton dissociation efficiency and resulting in a higher short-circuit current density (J_{SC}).

Both **GT57** and **GT60** exhibit strong absorption in the visible region and possess similar molecular backbones; however, their photovoltaic performances differ slightly, with **GT57** yielding a slightly lower PCE than **GT60**. The small participation of sulfur atoms in the frontier molecular orbitals may influence the charge separation dynamics, leading to a slightly larger band gap and thus an enhanced PCE conversion. Nevertheless, the difference is so small that both exhibit comparable performance. Furthermore, TD-DFT calculations indicate subtle differences in excited-state behavior.

More broadly, the modest PCEs ($\sim$4%) of both systems reflect several limiting factors beyond intrinsic molecular properties. While bulky *tert*-butyl and *tert*-butylthio groups enhance solubility and suppress aggregation, they may also hinder close π–π stacking, which is critical for efficient charge carrier mobility. In addition, potential mismatch in energy level alignment or unfavorable domain sizes within the bulk heterojunction may lead to charge recombination or inefficient exciton dissociation.

To enhance the photovoltaic performance of such ZnPc dimers, further molecular engineering is warranted. Strategies such as modifying the bridge (*e.g.*, incorporating more planar or electron-donating linkers), introducing push–pull architectures
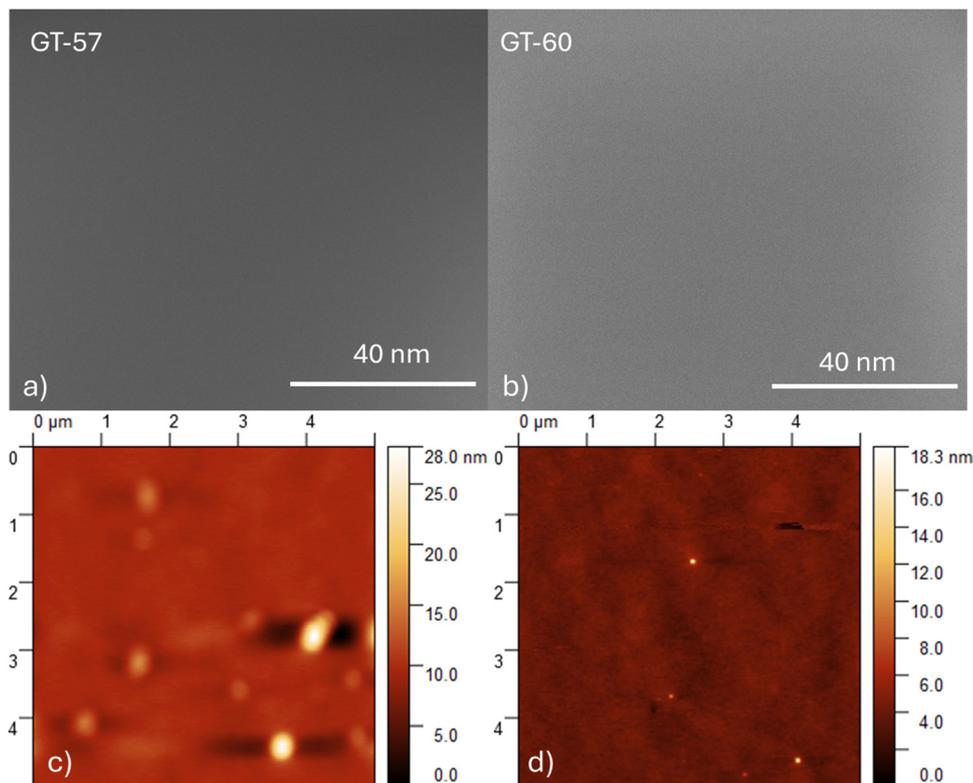
Fig. 9   SEM images of (a) **GT57** (b) **GT60** films on quartz substrate. AFM images of (c) **GT57** (d) **GT60** films on the quartz substrate.

to improve charge separation, or tailoring the side chains to modulate packing and morphology could be explored. Moreover, the use of alternative acceptors (*e.g.*, non-fullerene acceptors) and post-processing optimization (*e.g.*, thermal or solvent vapor annealing) could improve the active layer morphology and device efficiency. These directions will be central to our ongoing efforts toward developing next-generation ZnPc-based donor materials for organic photovoltaics.

Conclusion

This study reports the design and synthesis of two novel dimeric zinc phthalocyanines, **GT57** and **GT60**, incorporating bulky *tert*-butyl and *tert*-butylthio substituents. The two phthalocyanine units are connected *via* a 1,4-bis(2-ethylhexyloxy)-2,5-diethylbenzene linker. These molecules were studied to evaluate their effectiveness as donor materials in bulk heterojunction (BHJ) solar cell devices. Solar cells fabricated from a thin evaporated layer of dimeric ZnPcs and a spin-coated layer show short-circuit current densities of $\sim$1.4 mA cm^{-2} with open circuit voltages $\sim$200 mV under 100 mW cm^{-2} simulated AM 1.5 illumination. The electrochemical analysis and optical properties indicated that all synthesized phthalocyanine derivatives possess appropriate HOMO–LUMO band gap levels for BHJ solar cell applications, which theoretical calculations have further confirmed. The theoretical electronic structures are in good agreement with experimental findings regarding molecular orbital energies. The spectra calculated *via* TD-DFT enable us to assess the key spectral features of the newly

designated dimeric zinc phthalocyanines. This study opens new avenues for utilizing Pc dimers as efficient, stable, and cost-effective hole-transporting materials. Ongoing research is focused on reducing recombination phenomena and optimizing device performance.

Previous dimeric phthalocyanines (ZnPcs) faced significant challenges such as weak electronic coupling, poor charge separation, and fast charge recombination, primarily due to the use of flexible or non-conjugated linkers. These limitations hindered their efficiency in solar energy conversion applications. Additionally, the synthesis of dimeric ZnPcs often involves issues like purification difficulties, solubility, and aggregation, which adversely affect the device structure and performance. Addressing these challenges is crucial for optimizing the final product and improving its efficiency in electronic applications.

In this study, 2-ethylhexyloxy ($-OCH_2CH(C_2H_5)C_4H_9$) substituents were used as bridges to facilitate ease of solubility and electronic transitions. Additionally, bulky *tert*-butyl and *tert*-butylthio groups were employed to prevent aggregation. These structures, as phthalocyanine functional groups, were utilized to enhance donor properties, minimize challenges in synthesis and purification processes, and optimize solubility. Compared to previous studies, this approach demonstrated improved efficiency, making it a more promising strategy for dimeric ZnPcs.

Author contributions

Gülenay Tunç: investigation, formal analysis, visualization, writing – original draft. Gizem Gümüşgöz Çelik: formal

analysis, validation, visualization, writing – original draft. Betül Canımkurbey: investigation, formal analysis, visualization, writing – original draft. Burcu Dedeoğlu: methodology, writing – original draft, writing – review & editing. Ayşe Gül Gurek: methodology, writing – original draft, writing – review & editing, supervision, funding acquisition. All authors have read and agreed to the published version of the manuscript.

Data availability

The data that support the findings of this study are available from the corresponding author upon reasonable request. The data are not publicly available due to participant privacy and ethical considerations. Any additional data or materials can be provided upon request to ensure transparency and reproducibility of the research.

Conflicts of interest

The authors declare that the are no competing financial interests or personal relationships that could have appeared to influence the work reported in this paper.

Acknowledgements

References

1 K. M. Kadish, K. M. Smith, Â. S. Gabriel and R. Guilard, *The Porphyrin Handbook*, 1st edn, 2002, vol. 7.

2 M. V. Martínez-Díaz, G. De La Torre and T. Torres, *Chem. Commun.*, 2010, **46**, 7090–7108.

3 M. G. Walter, A. B. Rudine and C. C. Wamser, *J. Porphyrins Phthalocyanines*, 2010, **14**, 759–792.

4 H. Imahori, T. Umeyama, K. Kurotobi and Y. Takano, *Chem. Commun.*, 2012, **48**, 4032–4045.

5 F. Silvestri, I. López-Duarte, W. Seitz, L. Beverina, M. V. Martínez-Díaz, T. J. Marks, D. M. Guldi, G. A. Pagani and T. Torres, *Chem. Commun.*, 2009, 4500–4502.

6 A. Varotto, C. Y. Nam, I. Radivojevioc, J. P. C. Tomé, J. A. S. Cavaleiro, C. T. Black and C. M. Drain, *J. Am. Chem. Soc.*, 2010, **132**, 2552–2554.

7 Q. Wang, Y. Li, X. Yan, M. Rathi, M. Ropp, D. Galipeau and J. Jiang, *Appl. Phys. Lett.*, 2008, **93**(7), 073303.

8 A. Sánchez-Díaz, R. Pacios, U. Muñecas, T. Torres and E. Palomares, *Org. Electron.*, 2011, **12**, 329–335.

9 M. K. R. Fischer, I. López-Duarte, M. M. Wienk, M. V. Martínez-Díaz, R. A. J. Janssen, P. Bäuerle and T. Torres, *J. Am. Chem. Soc.*, 2009, **131**, 8669–8676.

10 M. Pegu, D. Molina, M. J. Álvaro-Martins, M. Castillo, L. Ferrer, P. Huang, S. Kazim, Á. Sastre-Santos and S. Ahmad, *J. Mater. Chem. C*, 2022, **10**, 11975–11982.

11 Á. J. Jiménez, F. Spanig, M. S. Rodríguez-Morgade, K. Ohkubo, S. Fukuzuml, D. M. Guldi and T. Torres, *Org. Lett.*, 2007, **9**, 2481–2484.

12 H. Ali and J. E. Van Lier, *J. Porphyrins Phthalocyanines*, 2014, **18**, 991–997.

13 C. C. Leznoff and A. B. P. Lever, *Wiley: Phthalocyanines Prop. Appl.*, 1996, vol. 1–4, 1568.

14 G. De La Torre, P. Vázquez, F. Agulló-López and T. Torres, *J. Mater. Chem.*, 1998, **8**, 1671–1683.

15 M. Hanack and H. Heckmann, *Eur. J. Inorg. Chem.*, 1998, 367–373.

16 G. De La Torre, T. Torres and F. Agulló-López, *Adv. Mater.*, 1997, **9**, 265–269.

17 C. C. Leznoff, H. Lam, S. M. Marcuccio, W. A. Nevin, P. Janda, N. Kobayashi and A. B. P. Lever, *J. Chem. Soc., Chem. Commun.*, 1987, 699–701.

18 N. Kobayashi, M. Numao, R. Kondo, S. ichiro Nakajima and T. Osa, *Inorg. Chem.*, 1991, **30**, 2241–2244.

19 D. Lelièvre, L. Bosio, J. Simon, J. J. André and F. Bensebaa, *J. Am. Chem. Soc.*, 1992, **114**, 4475–4479.

20 D. Lelievre, O. Damette and J. Simon, *J. Chem. Soc., Chem. Commun.*, 1993, 939–940.

21 J. Yang and M. R. Van De Mark, *Tetrahedron Lett.*, 1993, **34**, 5223–5226.

22 N. Kobayashi, P. Janda, H. Lam, W. A. Nevin, C. C. Leznoff, T. Koyama, A. Monden and H. Shirai, *J. Am. Chem. Soc.*, 1994, **116**, 879–890.

23 N. Kobayashi, Y. Higashi and T. Osa, *J. Chem. Soc., Chem. Commun.*, 1994, 1785–1786.

24 S. Vigh, H. Lam, P. Janda, A. B. P. Lever, C. C. Leznoff and R. L. Cerny, *Can. J. Chem.*, 1991, **69**, 1457–1461.

25 E. M. Maya, P. Vázquez and T. Torres, *Chem. – Eur. J.*, 1999, **5**, 2004–2013.

26 E. Göransson, J. Boixel, J. Jero Me Fortage, D. Jacquemin, H.-C. Becker, E. Blart, L. Hammarströ and F. Odobel, *Inorg. Chem.*, 2012, **51**, 11500–11512.

27 Y. H. Chiang, H. H. Chou, W. T. Cheng, Y. R. Li, C. Y. Yeh and P. Chen, *ACS Energy Lett.*, 2018, **3**, 1620–1626.

28 D. Molina, M. A. Ruiz-Preciado, F. Sadegh, M. J. Álvaro-Martins, M. Grätzel, A. Hagfeldt and Á. Sastre-Santos, *J. Porphyrins Phthalocyanines*, 2019, **23**, 546–553.

29 D. Molina, M. A. Ruiz-Preciado, B. Carlsen, F. T. Eickemeyer, B. Yang, N. Flores-Díaz, M. J. Álvaro-Martins, K. Nonomura, A. Hagfeldt and Á. Sastre-Santos, *ChemPhotoChem*, 2020, **4**, 307–314.

30 A. C. Yüzer, G. Kurtay, T. Ince, S. Yurtdaş, E. Harputlu, K. Ocakoglu, M. Güllü, C. Tozlu and M. Ince, *Mater. Sci. Semicond. Process.*, 2021, **129**, 105777.

31 M. M. Stylianakis, D. Konios, G. Viskadouros, D. Vernardou, N. Katsarakis, E. Koudoumas, S. H. Anastasiadis, E. Stratakis and E. Kymakis, *Dyes Pigm.*, 2017, **146**, 408–413.

32 H. Usta, D. Alimli, R. Ozdemir, E. Tekin, F. Alkan, R. Kacar, A. G. Altas, S. Dabak, A. G. Gürek, E. Mutlugun, A. F. Yazici and A. Can, *J. Mater. Chem. C*, 2020, **8**, 8047–8060.

33 S. Kaipova, H. Dinçer and A. Altindal, *J. Coord. Chem.*, 2015, **68**, 717–731.

34 H. Usta, D. Alimli, R. Ozdemir, S. Dabak, Y. Zorlu, F. Alkan, E. Tekin and A. Can, *ACS Appl. Mater. Interfaces*, 2019, **11**, 44474–44486.

35 H. Uchida, H. Tanaka, H. Yoshiyama, P. Y. Reddy, S. Nakamura and T. Toru, *Synlett*, 2002, 1649–1652.

36 G. Tunç, E. Güzel, I. Şişman, V. Ahsen, G. Cárdenas-Jirón and A. G. Gürek, *New J. Chem.*, 2019, **43**, 14390–14401.

37 H. Ali and J. E. Van Lier, *Tetrahedron Lett.*, 2014, **55**, 4163–4167.

38 K. M. Kadish, K. M. Smith, Â. S. Gabriel and R. Guilard, *The Porphyrin Handbook*, Academic press, Boston, 1st edn, 2002, vol. 7.

39 G. Gümüşgöz Çelik, A. N. Şahin, F. Lafzi, N. Saracoglu, A. Altındal, A. G. Gürek and D. Atilla, *Dalton Trans.*, 2022, **51**, 9385–9396.

40 E. T. Saka, M. Durmuş and H. Kantekin, *J. Organomet. Chem.*, 2011, **696**, 913–924.

41 L. Kaestner, M. Cesson, K. Kassab, T. Christensen, P. D. Edminson, M. J. Cook, I. Chambrier and G. Jori, *Photochem. Photobiol.*, 2003, **2**, 660–667.

42 M. J. Frisch, G. W. Trucks, D. J. Fox, H. B. Schlegel, G. E. Scuseria, M. A. Robb, J. R. Cheeseman, G. Scalmani, V. Barone, B. Mennucci, G. A. Petersson, H. Nakatsuji, M. Caricato, X. Li, H. P. Hratchian, A. F. Izmaylov, J. Bloino, G. Zheng, J. L. Sonnenberg, M. Hada, M. Ehara, K. Toyota, R. Fukuda, J. Hasegawa, M. Ishida, T. Nakajima, Y. Honda, O. Kitao, H. Nakai, T. Vreven, J. A. Montgomery Jr., J. E. Peralta, F. Ogliaro, M. Bearpark, J. J. Heyd, E. Brothers, K. N. Kudin, V. N. Staroverov, R. Kobayashi, J. Normand, K. Raghavachari, A. Rendell, J. C. Burant, S. S. Iyengar, J. Tomasi, M. Cossi, N. Rega, J. M. Millam, M. Klene, J. E. Knox, J. B. Cross, V. Bakken, C. Adamo, J. Jaramillo, R. Gomperts, R. E. Stratmann, O. Yazyev, A. J. Austin, R. Cammi, C. Pomelli, J. W. Ochterski, R. L. Martin, K. Morokuma, V. G. Zakrzewski, G. A. Voth, P. Salvador, J. J. Dannenberg, S. Dapprich, A. D. Daniels, Ö. Farkas, J. B. Foresman, J. V. Ortiz, J. Cioslowski and D. J. Fox, Gaussian Inc., Wallingford, Wallingford CT, 2013.

43 C. Lee, W. Yang and R. G. Parr, *Phys. Rev. B: Condens. Matter Mater. Phys.*, 1988, **37**, 785–789.

44 A. D. Becke, *J. Chem. Phys.*, 1993, **98**, 5648–5652.

45 A. D. Becke, *Phys. Rev. A: At., Mol., Opt. Phys.*, 1988, **38**, 3098–3100.

46 T. Yanai, D. P. Tew and N. C. Handy, *Chem. Phys. Lett.*, 2004, **393**, 51–57.

47 K. Jaffar, Z. M. Elqahtani, Q. Q. Afzal, M. Ans, S. Riaz, M. A. Tahir, J. Iqbal, Z. M. M. Mahmoud, Z. A. Alrowaili and M. S. Al-Buriahi, *Polymer*, 2022, **245**, 124675.

48 J.-D. Chai and M. Head-Gordon, *Phys. Chem. Chem. Phys.*, 2008, **10**, 6615–6620.

49 M. E. Casida, C. Jamorski, K. C. Casida and D. R. Salahub, *J. Chem. Phys.*, 1998, **108**, 4439–4449.

50 R. El Mouhi, A. Slimi, A. Fitri, A. T. Benjelloun, S. ElKhattabi, M. Benzakour, M. Mcharfi and M. Kurban, *Phys. B*, 2022, **636**, 413850.

51 R. El Mouhi, O. Daoui, A. Fitri, A. T. Benjelloun, S. El Khattabi, M. Benzakour, M. Mcharfi and M. Kurban, *New J. Chem.*, 2023, **47**, 812–827.

52 K. Harmandar, K. Granados-Tavera, M. Gezgin, M. Nebioğlu, İ. Şişman, G. Cárdenas-Jirón, D. Atilla and A. G. Gürek, *New J. Chem.*, 2022, **46**, 714–725.

53 E. Cancès, B. Mennucci and J. Tomasi, *J. Chem. Phys.*, 1997, **107**, 3032–3041.

54 B. Mennucci and J. Tomasi, *J. Chem. Phys.*, 1997, **106**, 5151–5158.

55 J. Tomasi, B. Mennucci and E. Cancès, *THEOCHEM*, 1999, **464**, 211–226.

56 B. Mennucci, E. Cancès and J. Tomasi, *J. Phys. Chem. B*, 1997, **101**, 10506–10517.

57 R. L. Martin, *J. Chem. Phys.*, 2003, **118**, 4775–4777.

58 A. M. Abdelghany, E. M. Abdelrazek, S. I. Badr and M. A. Morsi, *Mater. Des.*, 2016, **97**, 532–543.

59 W. H. Baek, H. Yang, T. S. Yoon, C. J. Kang, H. H. Lee and Y. S. Kim, *Sol. Energy Mater. Sol. Cells*, 2009, **93**, 1263–1267.

60 P. R. Berger and M. Kim, *J. Renewable Sustainable Energy*, 2018, **10**, 1.